Numerical Investigation of the Aerodynamic Performance for an Alternative Wing–Body–Tail Configuration

L. Smith,* K. J. Craig,† and J. P. Meyer‡
University of Pretoria, Pretoria 0002, South Africa
and
G. R. Spedding§
University of Southern California, Los Angeles, California 90089

DOI: 10.2514/1.C034595

It is common for new aircraft configuration proposals to include some kind of lifting body. The reduction in fuselage–wing interference drag, in principle, improves span efficiency and hence allows for reduction in total span and structural weight. One such proposal involves controlling body circulation by a central trailing-edge flap, and though the basic idea has been supported in initial wind tunnel tests, there have been no further attempts to systematically explore the design space for these wing–body–tail geometries. The first purpose of this study was to numerically simulate the experimental work. Simulations with incompressible Reynolds-averaged Navier–Stokes equations show quite significant separation over the aftbody, limiting the effectiveness of the trailing edge. The second purpose of the paper was to investigate the characteristics when two low-drag bodies from literature were used in otherwise similar wing–body–tail configurations. The wing–body–tail assemblages had different aftbody separation characteristics. Adding the trailing edge increased the total drag coefficient, and the expected improvement of induced drag did not lead to a net benefit. It is concluded that, if such a favourable geometry exists, then it has not been found here.

Nomenclature

A	=	wing planform area, m^2
AR	=	wing aspect ratio; b/c
b	=	tip-to-tip wingspan, m
C_D	=	drag coefficient
C_L	=	lift coefficient
c	=	chord length, m
D	=	drag force, N
d	=	maximum body diameter, m
L	=	lift force, N
l	=	body length, m
P	=	static pressure, Pa
P_{Total}	=	total pressure; $P + \rho U^2$, Pa
Re_c	=	Reynolds number based on wing chord; $\rho U c/\mu$
Re_l	=	Reynolds number based on body length; $\rho U l/\mu$
r	=	body radius, m
T_W	=	tail width, m
U	=	freestream velocity, m/s
$\|\|U\|\|$	=	velocity magnitude; $\sqrt{U_x^2 + U_y^2 + U_z^2}$, m/s
U_x	=	streamwise velocitsy component, m/s
U_y	=	cross-stream velocity component, m/s
U_z	=	vertical velocity component, m/s
x	=	streamwise direction, m
y	=	horizontal spanwise direction, m
y^+	=	nondimensional wall distance
z	=	verticle (wall-normal) direction, m
α	=	angle of attack, deg
δ	=	aftbody deflection angle, deg
μ	=	dynamic viscosity, kg/(m · s)
ρ	=	density, kg/m^3
τ_w	=	wall shear stress, Pa
ω	=	vorticity magnitude, 1/s

Received 26 May 2017; revision received 15 June 2018; accepted for publication 19 June 2018; published online 4 October 2018.

*Ph.D. Student, Department of Mechanical and Aeronautical Engineering; lelanie.smith@up.ac.za. Student Member AIAA (Corresponding Author).

†Professor, Department of Mechanical and Aeronautical Engineering; ken.craig@up.ac.za.

‡Professor, Department of Mechanical and Aeronautical Engineering; josua.meyer@up.ac.za. Member AIAA.

§Professor, Department of Aerospace and Mechanical Engineering; geoff@usc.edu. Member AIAA.

I. Introduction

A NUMBER of possible aircraft configurations attempt to reduce the wing–fuselage interference drag and loss of circulation over the central cargo-carrying body through lifting bodies [1], blended wing–bodies [2], and even flying wings [3,4]. One such recent proposal involved fitting a low-drag fuselage with a trailing-edge flap, whose deflection could modify the local circulation over the body and in one setting could match the circulation at the wing root. This fuselage design objective could be reconsidered if the fuselage is not required to carry a tailplane [5]. The design appeared to work as proposed in wind tunnel tests [6], but there was no attempt to optimize the geometry of the various components, and no corresponding computational tests were performed.

Thus, the three previous studies [6–8] have dealt with the characteristics of what we may term a baseline wing–body–tail configuration (WBT-0), with simply specified geometry and no special attention to separation control. Particle image velocimetry measurements were made for the WBT-0 at various aftbody deflection angles δ [6,7] and in [7] were compared with preliminary force balance measurements. Because of the lumped measurement of forces, it was not possible to identify the specific contributions of the various aerodynamic surfaces to the experimental global force coefficient. A computational study [8] used the Reynolds-averaged Navier–Stokes equations (RANS) (in the commercial code STAR-CCM+) to estimate the aerodynamic properties of the WBT-0. There was an increase in lift for increasing δ, which was even more pronounced when the tail, referred to as the Kutta Edge (KE) was added, but comcomitant drag penalty led to an overall reduction of the lift-to-drag ratio L/D in the KE configuration. In this respect, the conclusions of [7,8] did not entirely agree, but the error bars in [7] suggest that there was a significant amount of uncertainty for the experimental results.

In a preliminary attempt to bring specifically designed low-drag bodies (LDBs) into the design space, Smith et al. [9] conducted a

numerical study to investigate the effect of adding a KE to two LDBs whose properties have been well established in the technical literature [10,11]. LDBs are typically shorter and wider than a conventional fuselage, with the nose contours shaped to delay transition and aftbody contours to prevent separation. The combined effect can be a reduction of viscous and pressure drag. Initial experimental tests on KE deflection were always accompanied by aftbody deflection, and the same procedure was adopted in the numerical studies, so that tail deflection was achieved through deflection of the entire aftbody. This changes the geometry from the original low-drag specification but for the LDB-KE/NKEs (where NKE refers to no KE) [9], there were only small regions of recirculation over the aftbody with no complete separation. Aftbody deflection alone (with no tail) produced net positive lift, effectively adding camber to the previously axisymmetric outline. Though the lift increment was larger when a tail was added, the drag would also increase, and so net benefits in L/D would not necessarily be decisive. It was further noted that such measures were quite sensitive to details of separation over the body and tail, and paradoxically a preferred arrangement would be to locate the KE entirely within the bounds of the viscous wake [9].

The overall purpose of this study was to provide some insight into the differences between the previous experimental and numerical studies and to investigate a potential design space of the initially tested WBT configurations. This exploration of the design space was conducted by using 10 discrete WBT configurations (five δ with and without KE) for the WBT-0 at chord-based Reynolds number $Re_c = 10^5$ [6–8] and two LDBs at their specific design body length-based Reynolds number Re_l (1.2×10^6 for F-57 LDB and 10^7 for Myring LDB).

II. Numerical Modeling

A. Geometric Model and Mesh Generation

The wing–body–tail geometries have fineness ratios $l/d = 4.75$, 5.56, and 5.33, for the WBT-0, F-57, and Myring profiles, as shown in Fig. 1. A NACA 0012 section, rectangular wing with set angle of attack $\alpha = 6$ deg, $AR = b/c = 6.67$ was prescribed with a reduced chord length $0.98c$ for a numerically convenient blunt trailing edge. The wing leading edge was placed at $x/l = 0.4$ from the nose and $z/r = 0.8$ down from the largest vertical extent of the fuselage. Re_c was different in each case, based on the specific design Re_l for the LDBs ($Re_c = 2.7 \times 10^5$ and 2.4×10^6 for F-57 and Myring). In the six cases for each WBT-NKE/KE combination, the KE was set to have the same geometric ratios of tail width T_W to body diameter d and KE length, defined by two ratios l_1/l and l_2/l, shown in Fig. 2. The wings are also placed in the same geometric ratio to the reference WBT (the same horizontal and vertical distance away from the KE).

The WBT-0 was modeled in a simplified cylindrical shape representing the octagonal Dryden wind tunnel test section [6,7], which was a reasonable simplification because the difference in the lift and drag forces was only 0.25%. Modeling a wall boundary compared to having an open domain increased the force values approximately 2%, due to the blockage effects present when the walls were added. All solution domains were of half-models with a symmetry plane. The diameter of the wind tunnel is $4.5l$ (because $b/2 = 0.8l$, this leaves $1.45l$ as the distance to the wall from the wing tip), WBT-0 was positioned $6l$ from the inlet, and the total domain was $25l$, as shown in Fig. 3. Simulations of the wing alone and the body–tail (BT) alone were also done in the same domain. The domains for the F-57 and WBT-Ms had the same geometry as Fig. 3 with diameter at $3l$, and the test section length was $14l$ with the inlet $4l$ from the nose.

All bodies were meshed using the same mesh functions and boundary layer mesh growth rate as [8,9]. The WBT model had 15 boundary layer cells, and two cells on the outer wall boundary were sufficient for force predictions (without the wall cells, there is a 2% difference of the force values; there is a negligible difference in adding more than two cells there). The domain refinements were modeled in the same way as described in [8,9]. Additional refinements were placed around the wing and downstream of the wing into its wake. Figure 4 shows the mesh around the WBT-0 model.

The grid convergence index method [12] was used to ensure that drag estimates were not sensitive to further mesh refinement. All mesh sizes were in the order of $3–5 \times 10^6$, and the criterion $y^+ < 1$, which is a measure of boundary layer resolution, was satisfied for all cases.

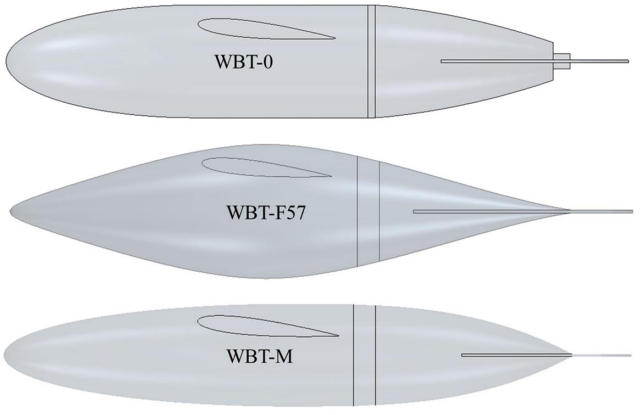

Fig. 1 F-57, Myring, and WBT-0 geometries.

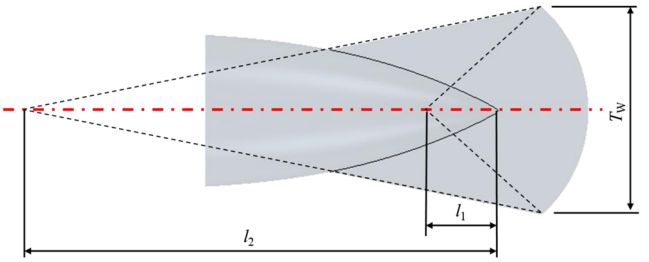

Fig. 2 KE width and length dimension relationships for all three WBTs.

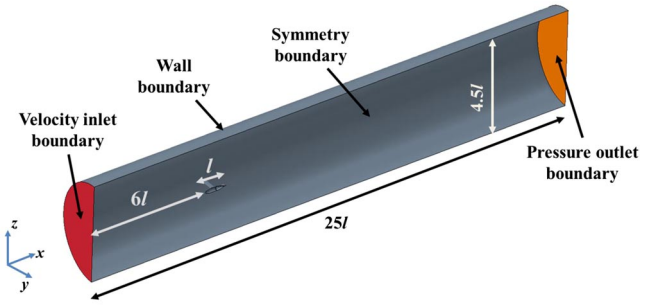

Fig. 3 Solution domain with coordinate system and boundary conditions for the WBT-0.

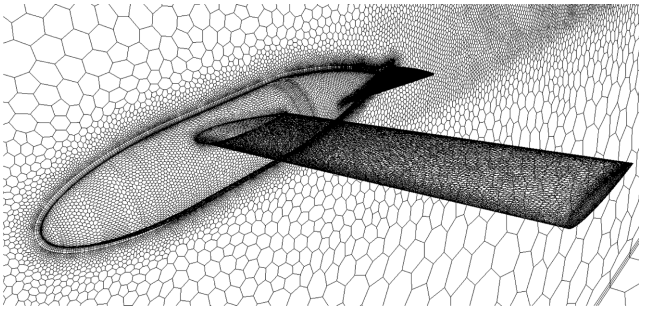

Fig. 4 Unstructured meshes around the WBT-0 model.

B. Boundary Conditions, Turbulence Model, and Transition Model

The flow was steady and incompressible, with constant-velocity inlet and outlet pressure boundary set at atmospheric (Fig. 3). The outer domains for the WBT-0 and-F57 were modeled as no-slip wall boundaries, whereas WBT-M had symmetry plane outer domain boundaries. The shear-stress transport (SST) $k-\omega$ turbulence model [13] coupled to a $\gamma - Re_\theta$ transition model [14] was selected as in [8,9]. The transition model is required for $Re < 10^6$, where laminar separation bubbles and transition become important to predict the aerodynamic forces with reasonable accuracy. All figures showing results from the computational fluid dynamics simulations are based on a steady converged RANS solutions. Even though this limits the ability to give specific insight on the exact flow features that could have been solved using unsteady simulations, the exact location and size of these features were not part of the purpose of this work.

III. Numerical Investigation of Experimental Observations

First, the global force values of the experimental model WBT-0 were considered, after which the flow mechanisms responsible for the force trends were investigated. Figure 5a shows the variation with δ of the pressure and friction drag coefficients components (normalized by wing planform area A, as is the standard for aircraft configurations) for the WBT-0. Drag coefficient C_D is defined as

$$C_D = \frac{D}{(1/2)\rho U^2 A} \tag{1}$$

where U is the freestream velocity, ρ is the density, and D is the drag force. Friction drag is almost unchanged at all δ, whereas pressure drag increases noticeably in the KE configuration. The WBT-0 C_D curves shows that a shallow minimum total drag for the KE condition occurs at $\delta = 2$ deg for KE and $\delta = 4$ deg for NKE.

Figure 5b shows that, in general, the lift coefficient C_L for the KE increases with δ, and it does so much faster than the NKE configuration. C_L is defined as

$$C_L = \frac{L}{(1/2)\rho U^2 A} \tag{2}$$

where L is the lift force. At $\delta = 0$ deg, C_L for both WBT-0-NKE/KE are lower than that of the wing alone because part of the wing span b is situated within the non-lifting fuselage. C_L of the WBT at $\delta = 5$ deg is about the same as for the NACA 0012 wing alone at $\alpha = 6$ deg. It is not obvious from the dissimilar scales of Figs. 5a and 5b, but the relative change in drag, $dC_D/C_{D,\delta=2\ \mathrm{deg}}$ is approximately 0.17 (taken between $\delta = 2$ deg and $\delta = 8$ deg), which is larger than the relative change in lift $dC_L/C_{L,\delta=2\ \mathrm{deg}}$ of approximately 0.11.

In Fig. 6, the normalized streamwise velocity U_x/U of the first boundary layer mesh cell, over the top of the body at $\delta = 4$ deg, shows the regions of recirculation indicated in dark blue on the color insert (the lower U_x/U value was restricted to zero to show negative velocities as a uniform dark blue section). For both the KE and NKE cases, there are large areas of recirculation over the aftbody, with separation occurring eventually at $x/l = 0.88$. Even though there are regions of recirculation over the top of the aftbody, the KE still shows attached flow over the largest part of its area. The pressure drag penalty due to the large sections of recirculation on the aftbody overshadows the gain of lift from the KE. These recirculation regions are common in low Reynolds number flowfields and specifically in bodies of revolution if the aftbody is not designed to avoid separation [10,15].

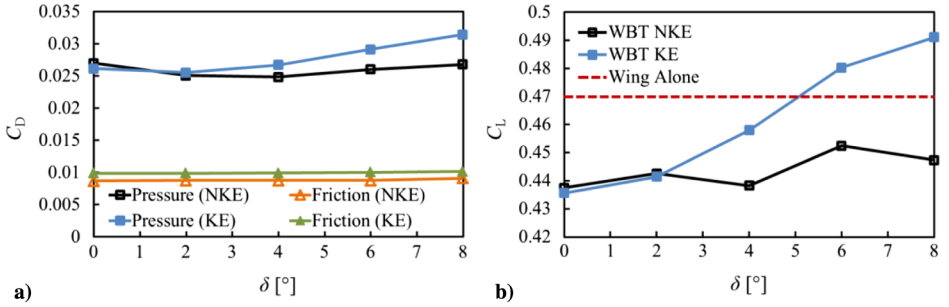

Fig. 5 Effect of varying δ on a) C_D, and b) C_L, for the WBT-0-NKE/KE.

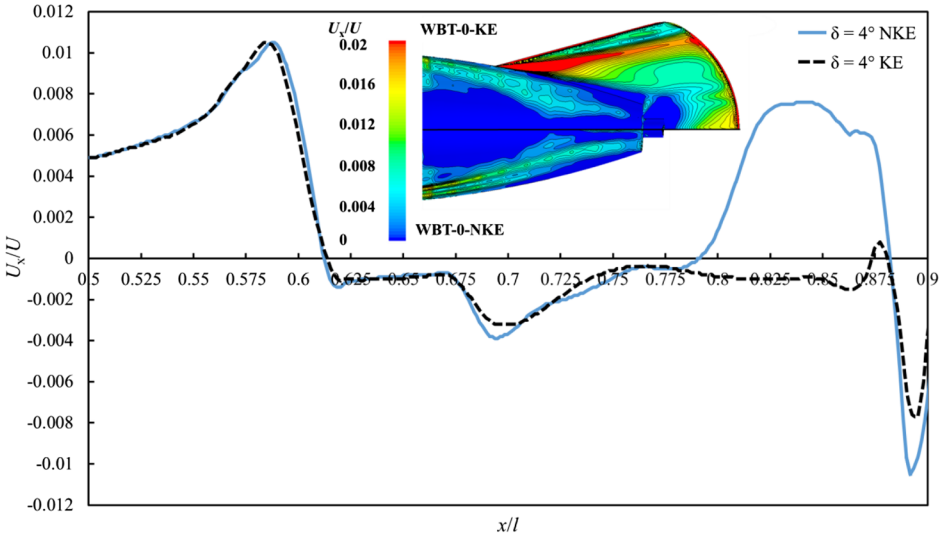

Fig. 6 U_x/U over the aftbody section ($0.5 < x/l < 0.9$) of the WBT-0-NKE/KE at $\delta = 4$ deg on the symmetry plane. Color insert shows the U_x/U contours over the top of the aftbody for the WBT-0-NKE/KE.

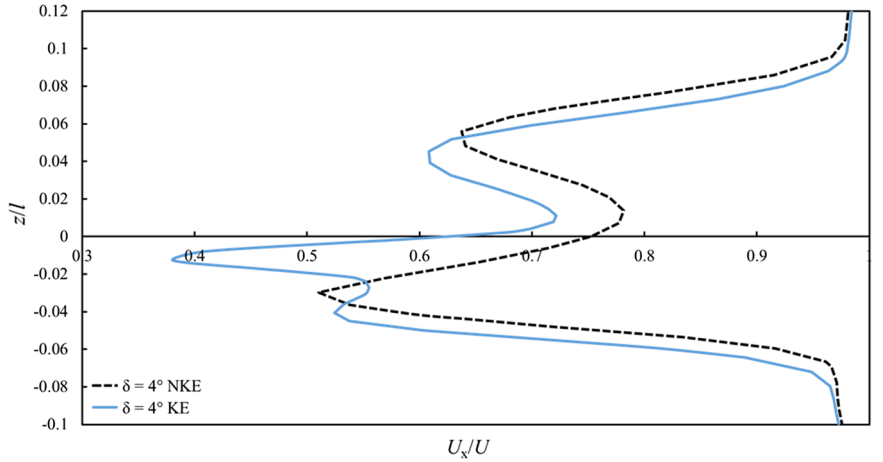

Fig. 7 U_x/U as the wake profile for the at $\delta = 4$ deg for the WBT-0-NKE/KE.

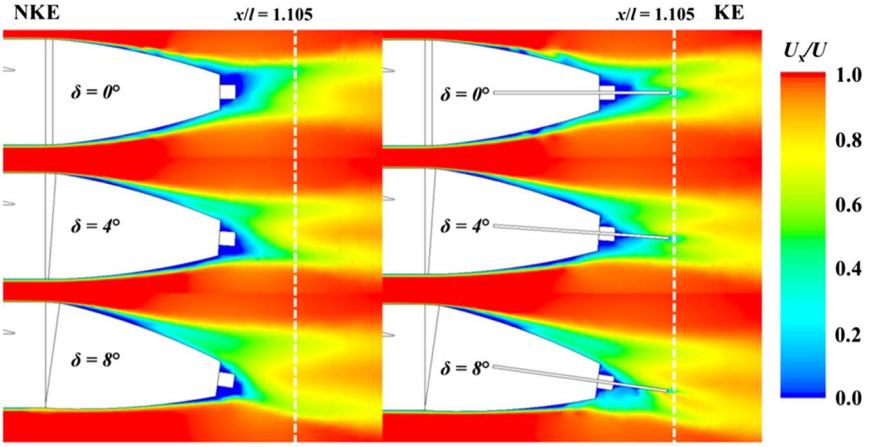

Fig. 8 U_x/U color contours on the symmetry plane at $\delta = 0$, 4, and 8 deg for the WBT-0-NKE/KE.

Figure 7 shows the wake velocity profile for $\delta = 4$ deg of the WBT-0-NKE/KE on the symmetry plane. There are three lobes present for the WBT-0-KE in the wake profile. The bottom and top lobes are due to the separation of the upper and lower boundary layers from the aftbody and the middle lobe the boundary layer over the KE. For the WBT-0-NKE, there are only two lobes for the bottom and top aftbody boundary layer separation. Both cases have a faster central U_x/U approximately at $z/l = 0.015$ due to the wing-induced wake. The same wake profiles are observed for other δ with Fig. 8 showing the U_x/U contours for $\delta = 0$, 4, and 8 deg on the symmetry plane. At $\delta = 0$ deg, the wake is deflected slightly upward even with the KE. This is due to the downwash of the wing, which then meets the upwash from the body, and the interaction creates an initial slight upwash in the near wake.

Figure 9 shows the P_{Total} contours (left) over the aftbody section at different locations for the WBT-0-NKE/KE. To visualize the complexity of the three-dimensional wake structure, vorticity magnitude ω isosurfaces with streamlines are shown in Fig. 9 (right). The isosurfaces are created by restricting the vorticity range to show only the viscous wake, and each color is made transparent with an opacity of 0.5. Figures 9a and 9b show the WBT-0-NKE/KE at $\delta = 0$ deg and Figs. 9c and 9d at $\delta = 4$ deg. The P_{Total} contours show lower values at the center of the vortices that are formed along the aftbody, and P_{Total} increases outward from these low points to create the curved path of the flow particles shown by the streamline plots. At both δ, there is an interaction between the boundary layer forming on the KE as well as the thickening of the boundary layer over the top and bottom of the aftbody, which is clear from the vorticity isosurfaces and streamlines. The wing-induced flowfield modifies the flow over the aftbody KE, and at $\delta = 0$ deg, the KE lies inside the deflected viscous wake behind the wing, which leads to complex interaction, and the leading-edge vortices on the top of the KE cannot form properly (compare Figs. 9b and 9d P_{Total} contours). At $\delta = 4$ deg, the downwash of the wing and thickening of the boundary layer over the aftbody adjust the effective angle of attack of the flow as it reaches the leading edges of the KE, and the vortex pair is formed on top of the KE. Ideally, the KE should be integrated into the aftbody to avoid the interaction with the wing-induced flowfield, and the aftbody KE should be shaped in a way such that there is no separation.

For comparative purposes, Figs. 10a and 10b show the P_{Total} contours over the aftbody of the BT-0-NKE/KE at $\delta = 0$ and 4 deg, to show the influence that the wing has on the downstream wake structure of the aftbody and KE. At $\delta = 0$ deg, the BT-0-NKE/KE both have a symmetrical wake structure, which is not the case for the WBT-0-NKE/KE in Figs. 9a and 9b. Also at $\delta = 4$ deg, there is a larger leeward P_{Total} for the BT-0-NKE/KE and a more gradual distrubtion spanwise across the KE than when the wing is added (Fig. 9d).

The overall objective of the KE is to restore the circulation over the (previously non-lifting) body so that the downwash distribution is 1) more uniform (lower induced drag), and 2) overall stronger so that the integrated total yields higher lift. The current geometry appears to be achieving some of these goals simply by body deflection alone, with no KE. Figure 11 shows the downwash distributions as the normalized cross-stream velocity, U_Z/U, along the normalized half-span ($2y/b$), behind the WBT-0-NKE/KE at each δ. The profiles were taken at $x/l = 1.105$ and $z/r = -1.5$, and the orange line indicates the position behind a NACA 0012 wing alone at $\alpha = 6$ deg. The wing tip is at $2y/b = 1$, and the KE ends at

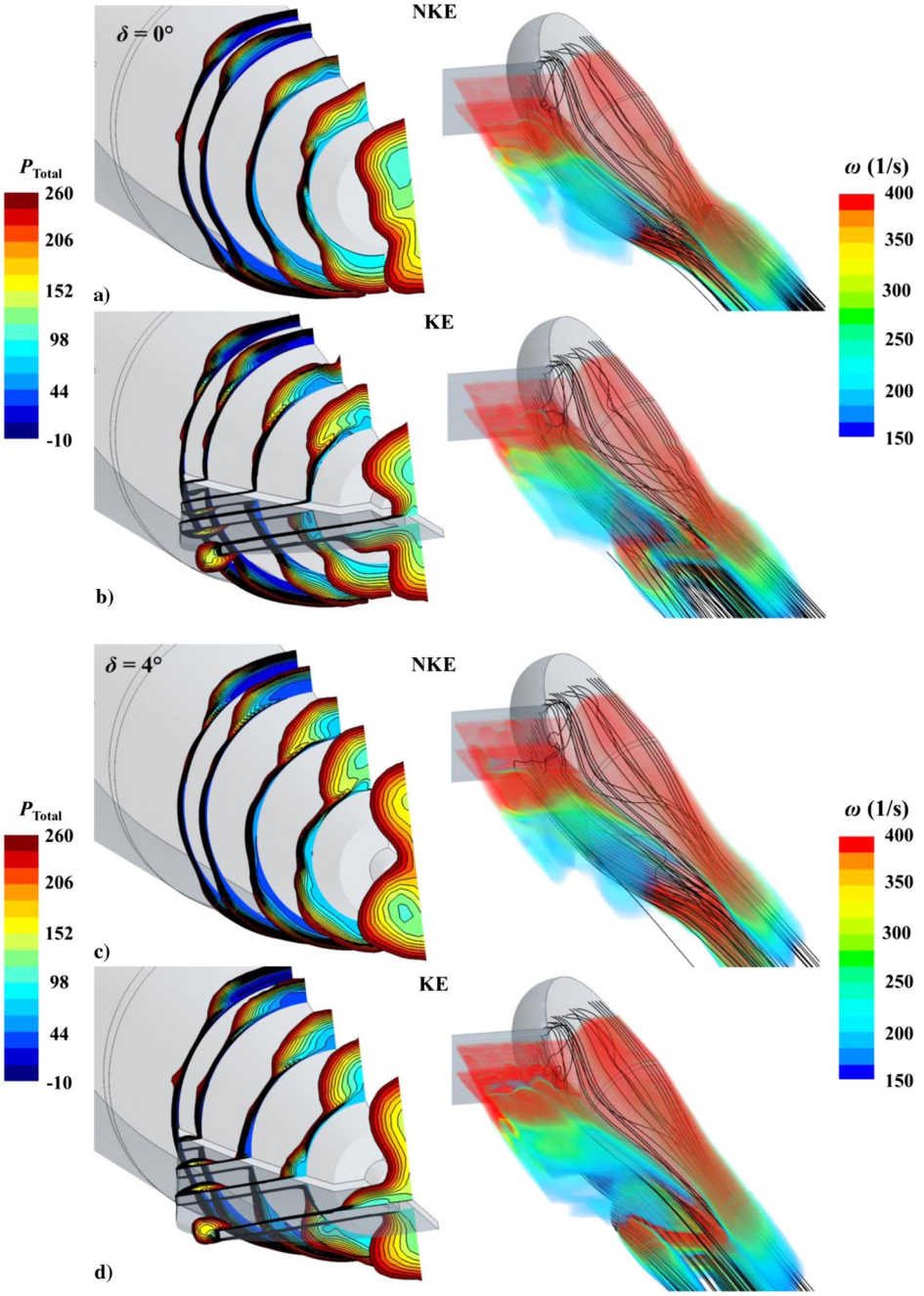

Fig. 9 P_{Total} contours at different streamwise locations over the aftbody (left) and vorticity isosurfaces and streamlines (right) for the WBT-0-NKE/KE at a,b) $\delta = 0$ deg, and c,d) at $\delta = 4$ deg.

approximately $2y/b = 0.17$. For all δ, there is a large spanwise variation at the center. At $\delta = 0$ deg, the KE configuration appears worse than the KE, with a greater downwash defect behind the body. This is due to the upwash from the body KE and downwash from the wing-induced wake interacting (cf. Fig. 8). When $\delta = 2$ deg, the KE and NKE have very little difference in downwash distribution, but as δ increases, the KE seems to offer an improvement. If the objective has been to restore the circulation profile to the wing-only case, then the KE can produce the downwash centrally but at the expense of having upwash around the KE tip. Clearly some careful matching would need to be done if a uniform downwash is to be achieved.

Figure 12 shows the U_z/U contour plots for $\delta = 0$, 4, and 8 deg at the same x/l location as the profiles in Fig. 11. There are multiple traces of upwash and downwash regions from the body and KE, and these will have to be reduced to obtain a uniform spanwise downwash, as shown by the wing-only U_z/U contour in Fig. 13.

Figure 14 shows a systematic breakdown of the lift provided by the body and KE relative to the wing-alone $C_L/C_{L,\text{wing}}$ of the WBT-0-NKE/KE as well as for the wingless case, BT-0. The WBT-0 body shows a larger increase in $C_L/C_{L,\text{wing}}$ than the BT-0 body because the wing that is added contributes to normal forces over the body to increase the overall lift. However, the KE has a reduction in the $C_L/C_{L,\text{wing}}$ when the wing is added due to the change of the effective angle of attack that the KE experiences from the upstream wing.

Even though the KE does seem to be a step in the right direction to restore the downwash distribution, its effectiveness is influenced by separation over the aftbody. Separation over the aftbody KE will lead to a drag penalty that outweighs this potential benefit. As an attempt to investigate the contribution of the aftbody design, two low-drag bodies from literature are used in the WBT.

IV. Numerical Investigation of Low-Drag Bodies in the Wing–Body–Tail

Figure 15a shows the variation of C_D with δ for the WBT-F57 and WBT-M, both in NKE/KE configurations. The C_L values for WBT-F57

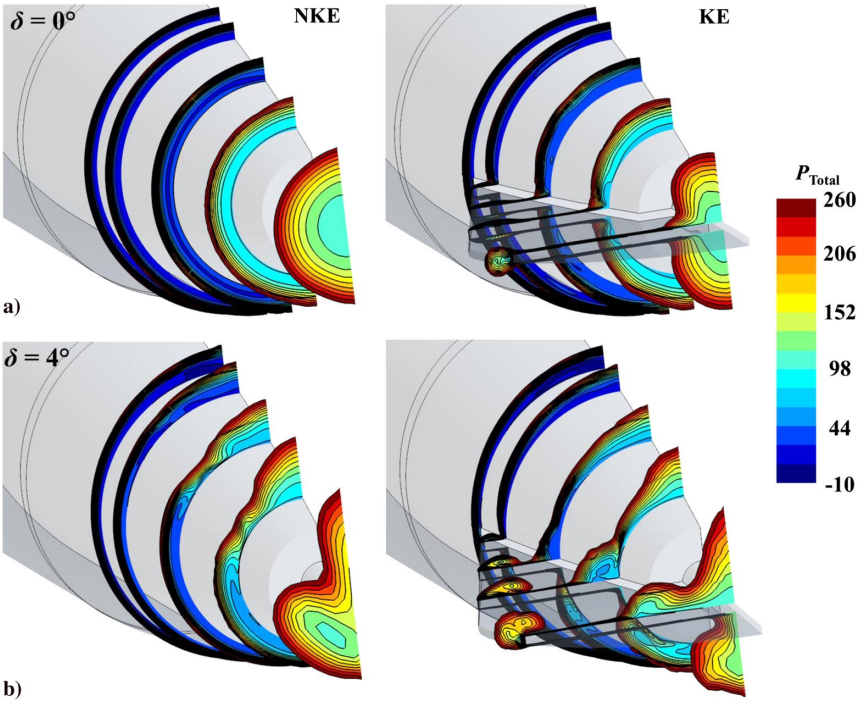

Fig. 10 P_{Total} **contours at the same location as Fig. 9 for BT-0-NKE/KE at a)** $\delta = 4$ **deg, and b)** $\delta = 0$ **deg.**

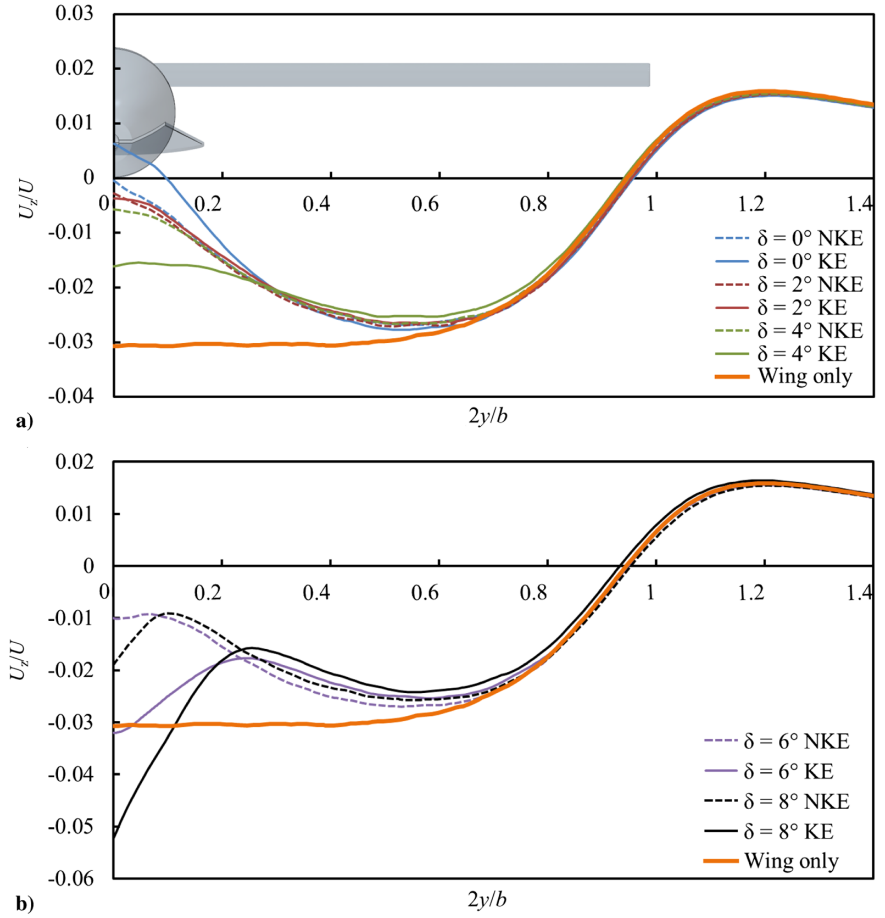

Fig. 11 Spanwise distribution U_z/U **at** $z/r = -1.5$ **and** $x/l = 1.105$ **as a function of** $2y/b$ **for the WBT-0-NKE/KE: a)** $\delta = 0$ **to 4 deg with a schematic of the WBT-0-KE, and b)** $\delta = 6$ **and 8 deg.**

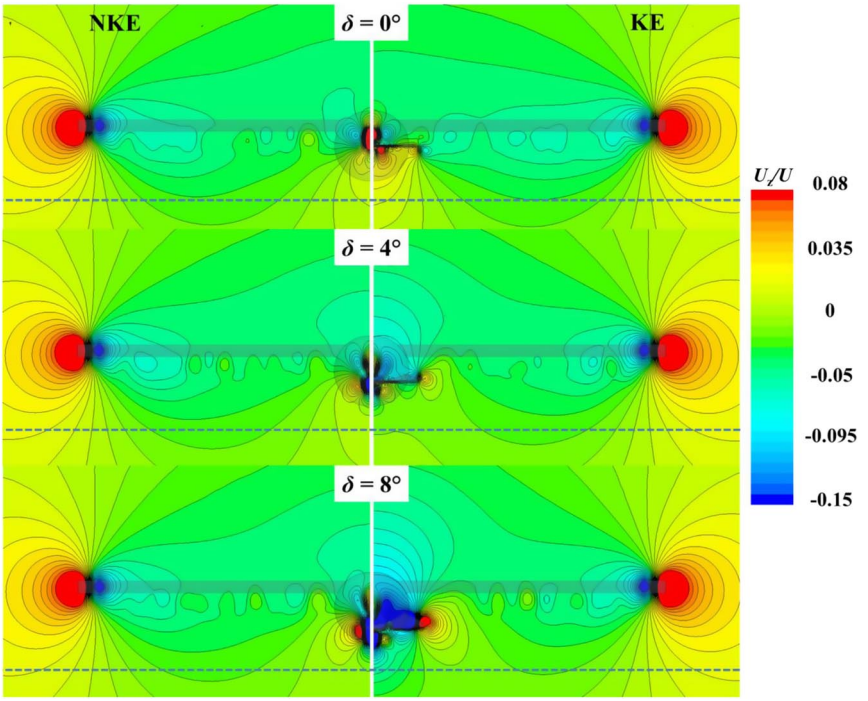

Fig. 12 U_z/U contours for the WBT-0-NKE/KE at $\delta = 0$, 4, and 8 deg. Dashed line indicating the location $z/r = -1.5$.

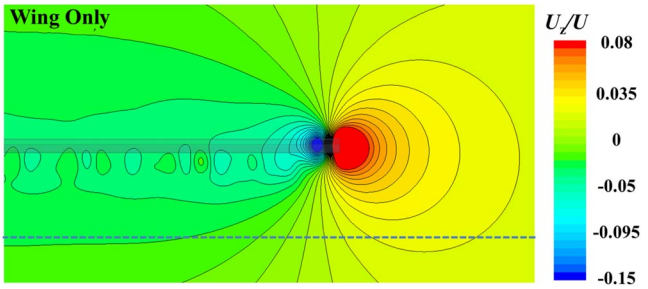

Fig. 13 U_z/U contours for the NACA 0012 wing alone. Dashed line indicating the location $z/r = -1.5$.

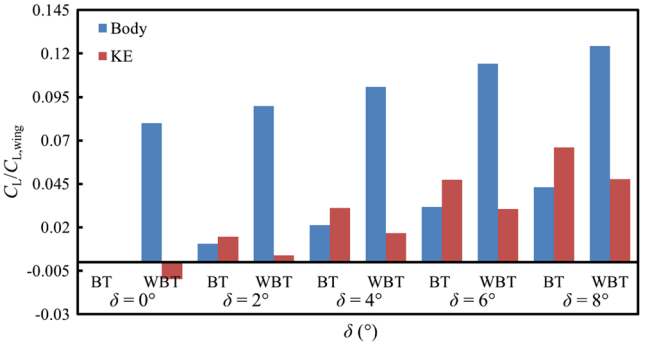

Fig. 14 $C_L/C_{L,\text{wing}}$ for the WBT-0-KE and BT-0-KE combinations at varying δ.

and WBT-M both show a linear increase as δ increases, similar to the WBT-0, as one might expect. C_L increases much more visibly with KE, and C_L has been restored almost to the wing alone value at $\delta > 3$ deg for WBT-F57-KE and at $\delta > 7$ deg for WBT-M-KE, as shown in Fig. 15b. The relative change in drag $dC_D/C_{D,\delta=2\text{ deg}}$ for the WBT-F57-KE is approximately 0.21 and for WBT-M-KE approximately 0.18, which is larger than their respective $dC_L/C_{L,\delta=2\text{ deg}}$ of approximately 0.12 and 0.09. All three WBTs share a similar trend in $dC_D/C_{D,\delta=2\text{ deg}}$, but the WBT-M-KE has the lowest C_D values overall. C_L increases for all three WBTs with the WBT-F57-KE at a higher rate than the WBT-0 and WBT-M-KE.

The reduction in the $dC_L/C_{L,\delta=2\text{ deg}}$ for the WBT-M compared to the WBT-F57-KE is attributed to the aftbody shape; where the WBT-F57 has a sharper taper, there is larger surface area of the KE exposed (approximately 26% more) that can provide a lift force than the more bluff Myring aftbody KE. However, Fig. 15a shows that the benefit in lift when considering the WBT-F57-KE is outweighed by the drag penalty. The F-57 and Myring LDB were originally designed to reduce drag [10] but not with wings attached. The F-57 LDB design focused on primarily transition delay to reduce drag, whereas the Myring LDB focused on the reduction of separation over the aftbody. Both LDBs have lower drag compared with the WBT-0-KE. Figure 16a shows color contours of U_x/U at $\delta = 0$, 4, and 8 deg for the WBT-F57-NKE/KE and Fig. 16b for WBT-M-NKE/KE. The vertical wake thickness is reduced when the KE is added, and the downward deflection of the wake increases with increasing δ in both cases. This was not clear in Fig. 8 of the WBT-0, and overall all the wake thicknesses of the WBTs with LDBs are smaller, consistent with the observed reduction in drag. The WBT-F57 shows areas of separation (shown by the $U_x/U < 0$) over the aftbody similar to the WBT-0, more so for the NKE than KE, but these separation areas are smaller for the WBT-M-NKE/KE. Also, for all WBTs at $\delta = 0$ deg, there is an initial upwash deflection of the streamwise wake defect present as the downwash from the wings interacts with the upwash from the aftbody.

Figure 17 shows the streamwise velocity profiles U_x/U for $\delta = 4$ deg of the WBT-F57-NKE/KE with and without the wing. The velocity profiles and contours of $\|U\|$ both show that the wings cause the wake behind the body to thicken, as though separation were occurring farther upstream. There is little difference when the KE is present. With no wings, the KE appears to protrude upward through the thin wake (Fig. 17b), and with wings, it is always inside a presumed separated wake. It is clear that the wing has a direct and negative influence on the trailing-edge conditions, again emphasizing the importance of careful matching within the WBT when any sort of trailing-edge device is added or the aftbody deflected.

U_x/U for $\delta = 4$ deg of the WBT-M-NKE/KE and WBT-F57-NKE/KE are shown in Fig. 18. Color insert of the U contours on the symmetry plane for the WBT-M-NKE/KE with the white dash line indicating the location of the profiles. Again, the downward deflection of the wake is observed with the addition of the KE, and for

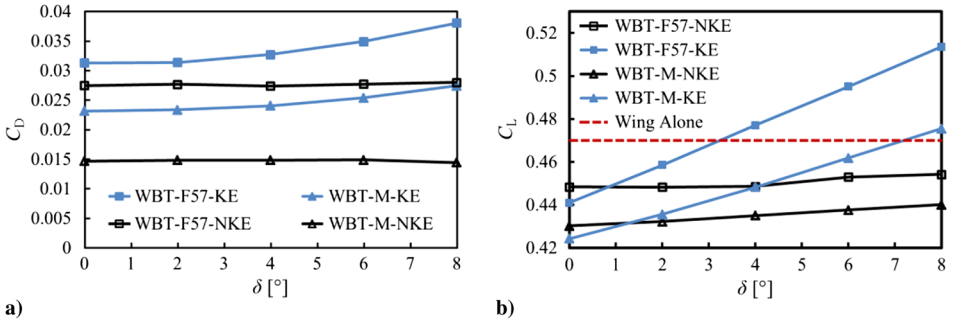

Fig. 15 Representations of a) drag coefficient C_D, and b) lift coefficient C_L, varying with δ for the WBT-F57 and WBT-M-NKE/KE.

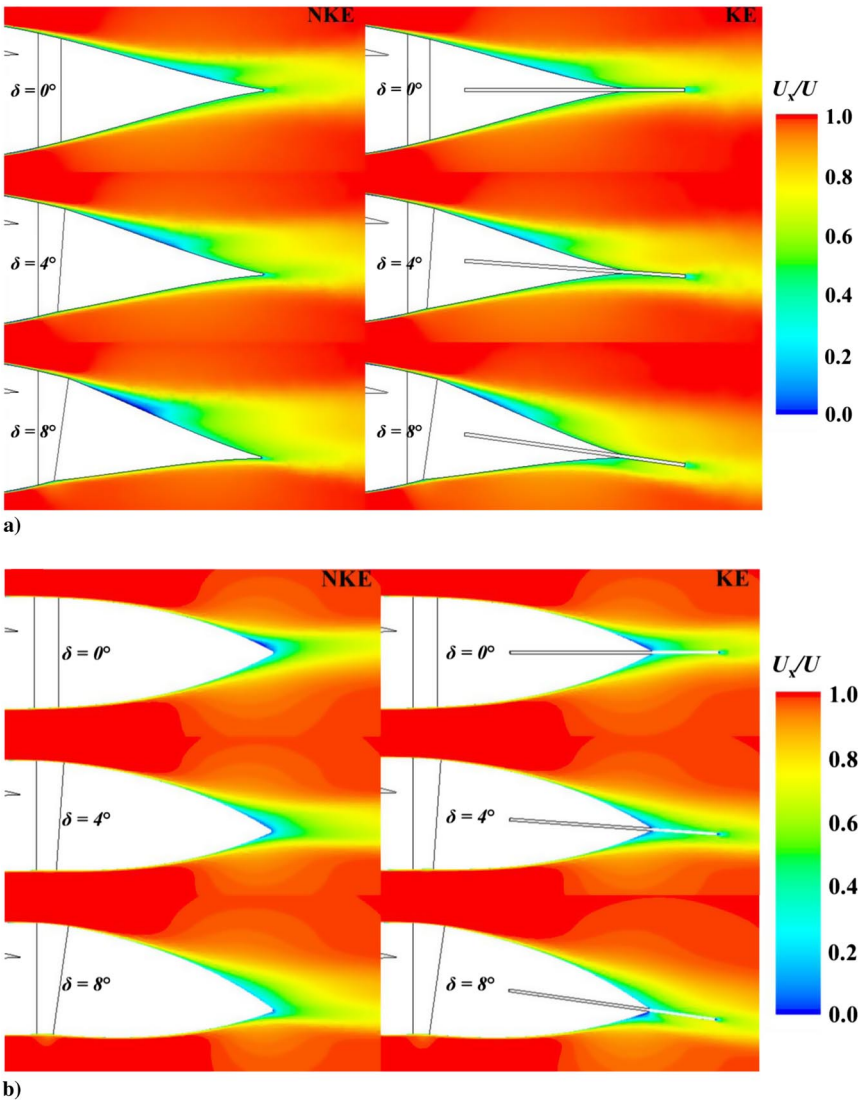

Fig. 16 U_x/U color contours for a) WBT-F57-NKE/KE, and b) WBT-M-NKE/KE, at $\delta = 0$, 4, and 8 deg.

the WBT-M, a double-lobe profile is not present, in contrast to the WBT-F57. The gradual aftbody taper to the sharp trailing edge of the WBT-F57 actually leads to premature separation on the aftbody when wings are present. The WBT-M has a smoother wake profile and a smaller wake defect, which explains the smaller pressure drag increase compared with the WBT-F57 in Fig. 15.

Figures 19a–19d shows the spanwise distribution for the WBT-F57 and WBT-M-NKE/KE at $\delta = 0$ to 8 deg. These values were extracted at the same streamwise location as for the WBT-0-NKE/KE. Similar to the WBT-0-NKE/KE in Fig. 11, the downwash profiles for $\delta = 0$ deg and KE show an increased upwash as the KE is immersed in a wing downwash, so that the the local KE incidence angle is negative, generating negative lift (Fig. 14). The WBT-F57-NKE has very little variation with changes in δ, possibly due to the more rapid termination of the aftbody of the F-57 LDB. For WBT-F57- and -M-KE, at $\delta > 6$ deg, the central downwash distribution of the wing alone is exceeded and much stronger than the WBT-0-KE, though uniform downwash distribution was never realized. Overall, WBT-F57 and -M show similar spanwise distributions, with $\delta = 2$ and 4 deg seeming most promsing.

Figures 20a and 20b show the U_z/U contours for the WBT-F57 and WBT-M-NKE/KE at $x/l = 1.105$, respectively, with the view direction and location of the contour plot shown at the top of Fig. 20. There are far fewer local upwash and downwash regions behind the

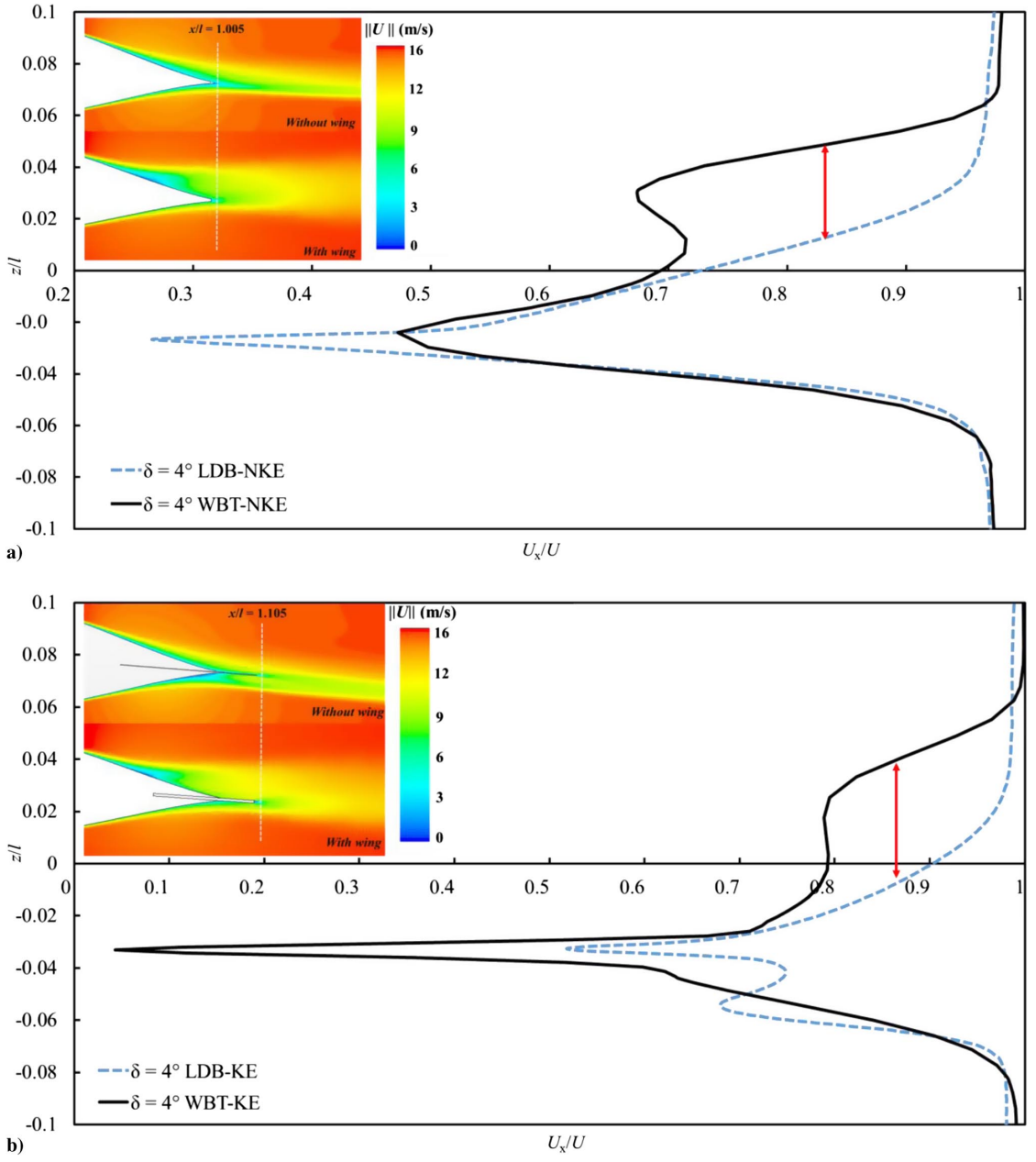

Fig. 17 U_x/U as the wake profile for the F-57 LDB and WBT a) without KE, and b) with KE at $\delta = 4$ deg. Red arrows indicate the difference between the wake profile with and without a wing.

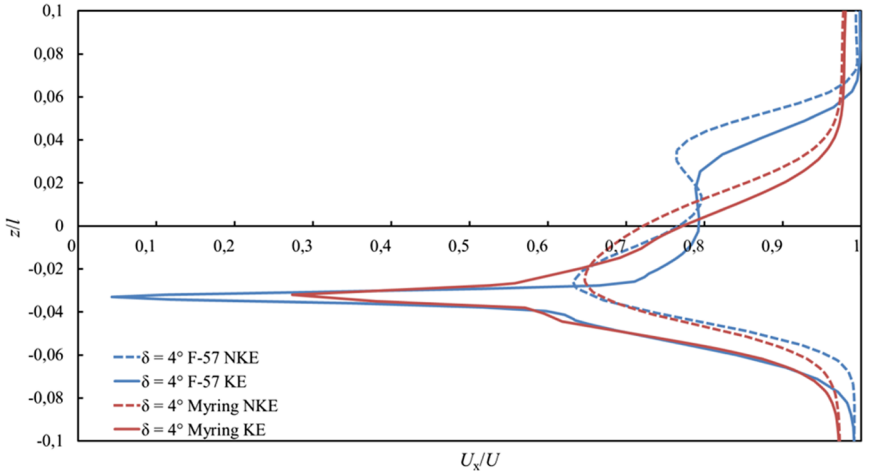

Fig. 18 U_x/U at $\delta = 4$ deg for the WBT-M-NKE/KE compared with the F57 WBT-NKE/KE.

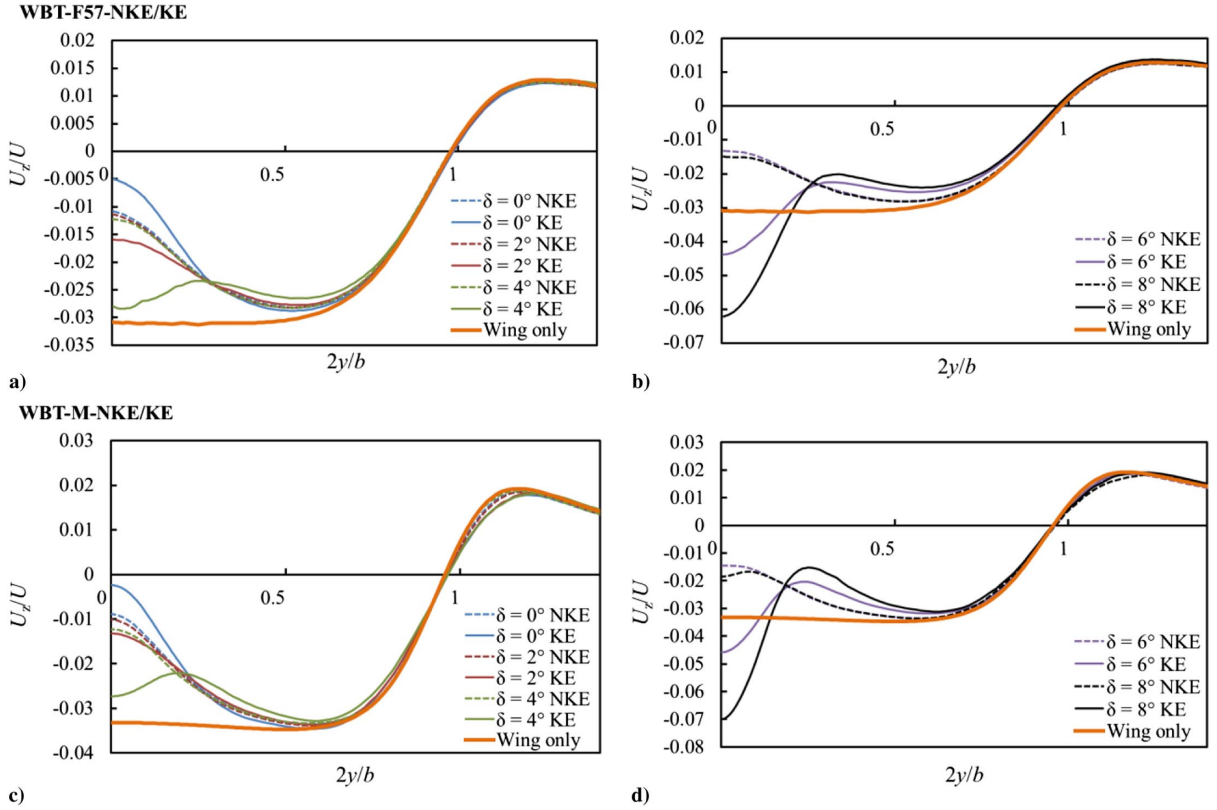

Fig. 19 U_z/U as a function of $2y/b$ for WBT-F57-NKE/KE, a) $\delta = 0$ to 4 deg, b) $\delta = 6$ and 8 deg; and for WBT-M-NKE/KE, c) $\delta = 0$ to 4 deg, and d) $\delta = 6$ and 8 deg, at the same location as Fig. 11.

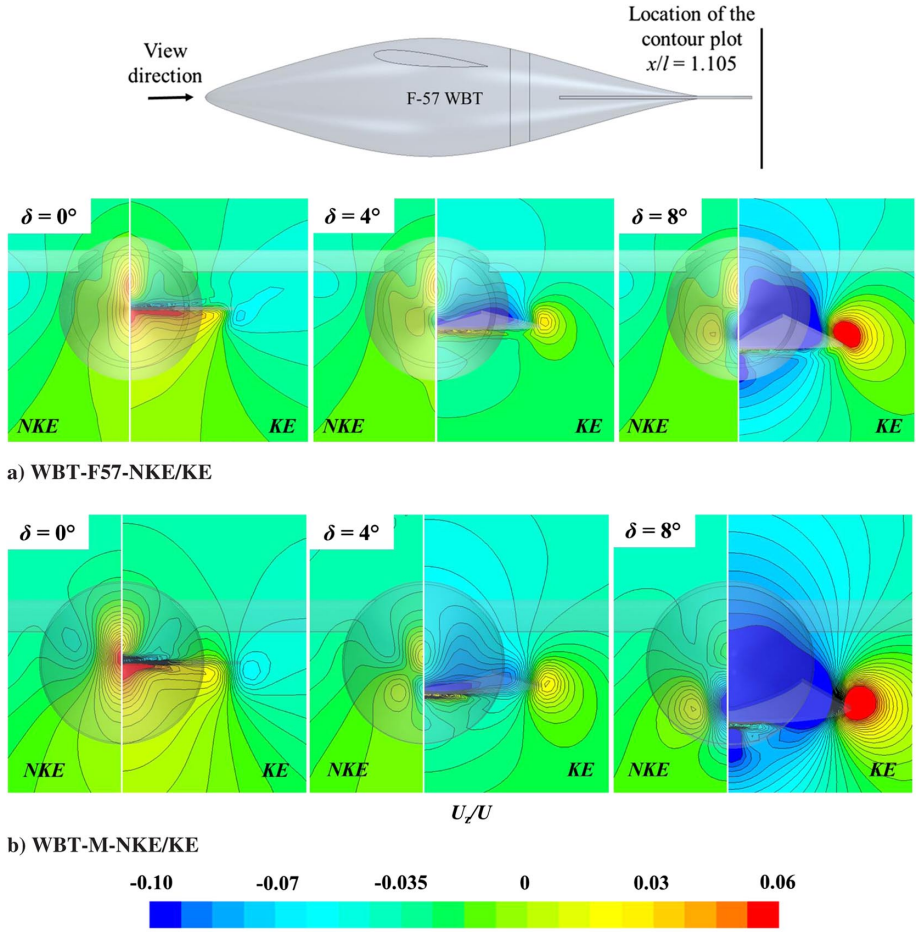

Fig. 20 U_z/U contours for a) WBT-F57-NKE/KE, and b) WBT-M-NKE/KE, at $\delta = 0$, 4, and 8 deg downstream at $x/l = 1.105$. The location of the contour plot as well as the view direction are shown at the top.

body and KE of the WBT-F57 and WBT-M-NKE/KE compared to the WBT-0-KE/NKE in Fig. 12. WBT-M-NKE/KE has a smaller and more central upwash region at $\delta = 0$ deg (Fig. 20b) than the WBT-F57-NKE/KE. However, at $\delta = 4$ and 8 deg, the WBT-M-NKE/KE has a larger central downwash region than the WBT-F57-NKE/KE.

V. Discussion

The WBT-0 aftbody was not designed to provide any pressure recovery or reduce separation over the afbody, and as a result the boundary layer separates, leading to a high-pressure drag and thick associated wake. For both the WBT-F57 and WBT-M-NKE/KE, the wakes have lower fluctuation in U_x/U, a reduced wake deficit, and lower pressure drag.

In terms of lift provided by the different WBT arrangements, Fig. 21 gives a breakdown of C_L relative to the $C_{L,\text{wing}}$ (based on the amount of lift provided by the wing alone) for the body and KE components. All of the WBT-KEs show (cf. Figs. 8 and 16) an upward deflection of the wake for the $\delta = 0$ deg, with the largest upward deflection seen at WBT-0 and WBT-F57-KEs. At all increasing δ, the WBT-KEs show an increase in lift on the body, with the WBT-F57-KE body showing a larger contribution compared to the other two WBT-KEs. The KEs of the two bluff bodies WBT-0 and WBT-M have a smaller lift contribution compared to the KE of WBT-F57, with an overall rate of increase that is smaller as well. This, as suggested before, is due to the sharper taper of the F-57 LDB leaving a larger surface area exposed and allowing the leading-edge vortices to develop without as much interference from the body vortices but as a consequence is more sensitive to the wing-induced downwash. The WBT-0 body shows a larger contribution in lift compared to the WBT-F57 body. The large contribution by the WBT-0 body is attributed to the strong upper and lower body vortices that developed over the aftbody.

Any given wing–fuselage geometry has a higher L/D for a simple body deflection (NKE) then with tail (KE) (Fig. 22). Though the KE adds lift, it does so with a drag cost that is relatively higher. For

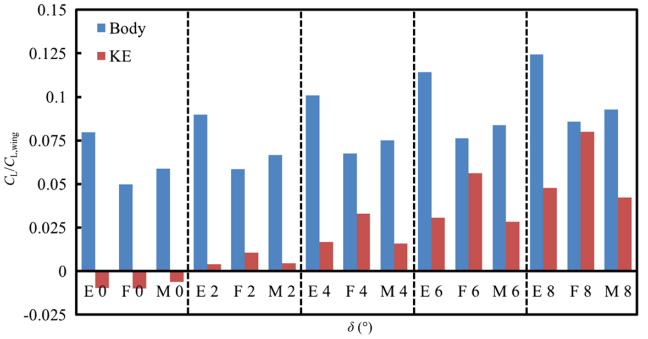

Fig. 21 $C_L/C_{L,\text{wing}}$ for the three WBT-KEs at varying δ (E refers to WBT-0).

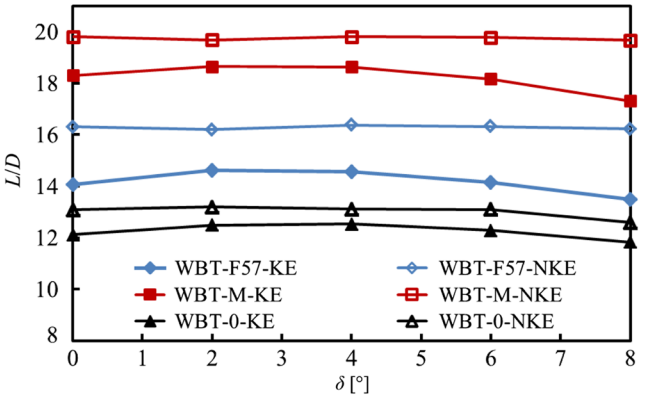

Fig. 22 Effect of varying δ on L/D for KE and NKE for all three WBT combinations.

increment in lift alone, the WBT-F57 seems to be the most feasible option (Fig. 15), but the drag increment reduces L/D, and so if this is the figure of merit, the WBT-M would be considered the best candidate to further explore.

Initial speculation in terms of successful implementation of the KE by [6] identifies that, with the fuselage contributing a portion of the lift, for a given design objective, the wing size could be reduced. This in turn will lead to an improved transport efficiency because the overall aircraft mass and wetted surface could be reduced. L/D is an incomplete measure of such total system benefits, and these design modifications may offer an overall benefit to the configuration that outweigh drag penalties observed here. L/D is also an incomplete measure of the aircraft design challenge, and no practical aircraft will emerge unless and until stability and control characteristics are correctly integrated. Of particular importance is the requirement to maintain both cruise efficiency and trim (specially in pitch). It would be very interesting to perform an optimisation study with a fully parameterized body of revolution at a given volume and flight speed to find a blended fuselage–KE geometry for low drag combined with constraints on pitch stability and control.

VI. Conclusions

This work confirms that the KE can influence the WBT wake structure, as initially estimated in experiment [6,7]. The results here suggest that the original Kutta edge tail concept requires careful matching in the reality of viscous flows over bodies and wings at finite Reynolds number. In particular, if the KE is wholly or partially immersed in a wake that derives from earlier upstream separation, then the KE cannot operate effectively, and the body termination conditions must already be judged to be suboptimal. If there is an optimal wing–body–tail configuration that leads to significant benefits in L/D, then it presumably would have to live in a domain where separation is almost completely avoided. The second modifying consideration is that if an entire system is designed for a certain lifting objective, then the option of providing that weight support through a modified geometry that includes a KE might not be well described by a single number such as L/D. When system benefits of reduced wing length, area, and weight are included (and subsequently fed back into the new design set point for C_L), the interlocked design benefits of each component might be difficult to isolate. The properties of the idealized WBT project with real bodies at finite Reynolds number are not easy to predict, and a helpful start might involve selected parameter sweeps that test design sensitivities close to realistic operating conditions, which might usefully include pitch stability and control as design constraints at the outset.

Acknowledgments

The authors would like to thank the South African National Aerospace Center and Airbus for their financial support with this research project.

References

[1] Drela, M., "Development of the D8 Transport Configuration," *29th AIAA Applied Aerodynamics Conference*, AIAA Paper 2011-3970, June 2011.

[2] Liebeck, R. H., Page, M. A., and Rawdon, B. K., "Blended-Wing–Body Subsonic Commercial Transport," *36th AIAA Aerospace Sciences Meeting and Exhibit*, AIAA Paper 1998-0438, 1998.

[3] Horton, R., and Selinger, P. F., *Nurflügel: Die Geschichte der Horten-Fluzeuge 1933–1960*, Weishaupt Verlag, Graz, Austria, 1987.

[4] Woolridge, E., *Winged Wonders: The Story of the Flying Wings*, Smithsonian Inst. Press, 1983.

[5] Agenbag, D. S., Theron, N. J., and Huyssen, R. J., "Pitch Handling Qualities Investigation of the Tailles Gull Wing Configuration," *Journal of Aircraft*, Vol. 46, No. 2, 2009, pp. 683–691. doi:10.2514/1.39755

[6] Huyssen, R. J., Spedding, G. R., Mathews, E. H., and Liebenberg, L., "Wing–Body Circulation Control by Means of a Fuselage Trailing Edge," *Journal of Aircraft*, Vol. 49, No. 5, 2012, pp. 1279–1289. doi:10.2514/1.C031543

[7] Davis, T. W., and Spedding, G. R., "Lift and Drag Measurements of a Gull-Wing Configuration Aircraft," *53rd AIAA Aerospace Sciences Meeting*, AIAA Paper 2015-0027, 2015.

[8] Smith, L., Craig, K. J., Meyer, J. P., and Spedding, G. R., "Numerical Simulations of a Proposed Wing–Body–Tail Configuration," *54rd AIAA Aerospace Sciences Meeting*, AIAA Paper 2016-0800, 2016.

[9] Smith, L., Craig, K. J., Meyer, J. P., and Spedding, G. R., "Modifying Low-Drag Bodies to Generate Lift: A Computational Study," *Journal of Aircraft*, Vol. 54, No. 3, 2017, pp. 1150–1161.

[10] Parsons, J. S., and Goodson, R. E., "Optimum Shaping of Axisymmetric Bodies for Minimum Drag in Incompressible Flow," Ph.D. Dissertation, Purdue Univ., West Lafayette, IN, 1972.

[11] Myring, D. F., "A Theoretical Study of the Effects of Body Shape and Mach Number on the Drag Bodies of Revolution in Subcritical Axisymmetric Flow," Royal Aircraft Establishment TR 8100, 1981.

[12] *Standard for Verification and Validation in Computational Fluid Dynamics and Heat Transfer*, ASME, New York, 2009.

[13] Menter, F. R., "Two-Equation Eddy-Viscosity Turbulence Models for Engineering Applications," *AIAA Journal*, Vol. 32, No. 8, 1994, pp. 1598–1605.
doi:10.2514/3.12149

[14] Menter, F. R., Langtry, R. B., Likki, S. R., Suzen, Y. B., Huang, P. G., and Volker, S., "A Correlation-Based Transition Model Using Local Variables Part 1—Model Formulation," *Journal of Turbomachinary*, Vol. 128, 2006, pp. 413–422.

[15] Smith, A. M. O., Stokes, R. T., and Lee, R. S., "Optimum Tail Shapes for Bodies of Revolution," *Journal of Hydronautics*, Vol. 15, Nos. 1–4, 1981, pp. 67–73.
doi:10.2514/3.48186